Alexandria Engineering Journal (2022) 61, 8897–8909

HOSTED BY

ELSEVIER

Alexandria University

Alexandria Engineering Journal

www.elsevier.com/locate/aej
www.sciencedirect.com

MIIM-based optical log spiral rectenna for efficient IR energy harvesting

Ali Yahyaoui [a,b], Ahmed Elsharabasy [c], Jawad Yousaf [d], Khaled Sedraoui [a,e,f], Hatem Rmili [a,e,f,*]

[a] *K. A. CARE Energy Research and Innovation Center, King Abdulaziz University, Jeddah 21589, Saudi Arabia.*
[b] *University of Tunis El Manar (UTM), National Engineering School of Tunis (ENIT), Communications Systems Laboratory (SysCom), BP 37, Belvédère 1002 Tunis, Tunisia*
[c] *Electrical and Computer Engineering Department, McMaster University, Hamilton ON L8S 4K1, Canada*
[d] *Department of Electrical, Computer, and Biomedical Engineering, Abu Dhabi University, United Arab Emirates*
[e] *Electrical and Computer Engineering Department, Faculty of Engineering, King Abdulaziz University, Jeddah, Saudi Arabia.*
[f] *Center of Research Excellence in Renewable Energy and Electrical Power Systems, King Abdulaziz University, Jeddah 21589, Saudi Arabia*

Received 25 October 2021; revised 21 January 2022; accepted 10 February 2022
Available online 26 February 2022

KEYWORDS

Photoconductive THz antenna;
Log spiral antenna;
MIIM diode;
Energy harvesting

Abstract This study proposed, for the first time, a newly developed metal–insulator-insulator–metal (MIIM)-based log-spiral rectenna for energy harvesting applications. The designed resonant log-spiral antenna at 28.3 THz forwards the absorbed infrared (IR) electromagnetic (EM) radiations to the installed double insulator-based MIIM rectifying diode. The realized MIIM diode is formed by sandwiching the two insulators among the designed resonant antenna terminals (hot spot region). Antenna terminals are used as the electrodes of the rectifying diode. This novel approach ensures the maximum transfer of captured IR EM radiations by the antenna to the rectifying part with good impedance matching and thus increases the overall conversions efficiency. The study presents an in-depth analysis of the impact of the changing metal types (Au, Al, Ag, and Cu) and insulating materials (Al_2O_3, Cu_2O, Ta_2O_5, TiO_2, and ZnO with10 different formations) on the realized rectenna performance in terms of captured E-field enhancement, I/V, resistivity, and responsivity characteristics. It is found that the overall performance of the proposed double insulator-based rectenna system is better for the asymmetric configuration of Au- Al_2O_3- Cu_2O –Cu and it exhibits 100% enhanced non-linearity as compared to MIM-based configuration.

1. Introduction

Sustainable green energy is the need of the future to meet the ever-increasing demand for power for industrials, households,

* Corresponding author.
E-mail address: hmrmili@kau.edu.sa (H. Rmili).
Peer review under responsibility of Faculty of Engineering, Alexandria University.

https://doi.org/10.1016/j.aej.2022.02.025
1110-0168

offices, and social applications. Owning to the rapid diminution of fossil fuels, more research is being conducted for the development of cheap and clean renewable energy from non-fossil fuel sources and increasing the efficiency of the existing energy harvesting mechanisms [1–3].

Sun is one of the major sources of renewable energy. The conventional photovoltaic (PV) technology only harvests the fraction of the total solar energy in the visible spectrum (380 nm – 780 nm) with lower conversion efficiency along with higher associated costs [2,3]. However more than half of the solar radiations, present in infrared (700 nm – 106 nm) region (IR) with maximum emissivity at 28.3 THz (10.6 μm peak wavelength), cannot be harvested using PV panels. IR rectennas are being developed for the harvesting of these bulk untapped electromagnetic (EM) radiations from the sun [4–8].

The process of energy harvesting using optical rectennas is illustrated in Fig. 1. The rectenna constitutes an antenna and a coupling rectifying diode. The antenna is designed to resonant at 28.3 THz for the capturing of maximum illuminating IR EM radiations from the sun. The rectifying diodes convert the coupling IR resonating signals from the antenna to the direct current (DC) level. The higher conversion efficiency of the IR rectenna systems demands good impedance matching between the antenna and rectifying diode at high frequency and high zero-bias responsivity (non-linear characteristics) of the diode [9 10].

The conventional employed Schottky diodes at microwave frequencies are not useful for the rectification of the high-frequency IR solar radiations due to their low-speed and high time constant. Metal-insulator–metal (MIM) diodes have been given preference for the IR rectification applications due to their near zero-bias operation, small size, ultrafast speed, CMOS compatibility, and high non-linearity characteristics [2,9]. Such properties of the MIM diodes are essential for the conversion of the small-amplitude input alternating current (AC) signal to DC levels at high frequency. The MIM diodes operate on the principle of quantum mechanical tunneling in which electrons tunnel from the first metallic layer to the second one through the sandwiching insulator within a few femtoseconds [9,10].

Several groups have designed various kinds of nano-antennas for IR energy harvesting applications. The investigated designs include dipole [4,11], slit [12], bowtie [4,5,7,11,13], dimer [14], two-wire split [8], and square patch [15] structures, to name a few. The RF and ambient energy harvesting concept are also well studied in [16–22]. In [16,18], authors reported a Hilbert-shaped metamaterial (MTM) array-based antenna on indium nickel oxide polymerized palm fiber and organic substrates respectively for the RF energy harvesting. The ultrawideband miniaturized microstrip-based structures are presented in [17,19] for harvesting applications in the RF frequency range. The study of [20] discussed that using multiport pixel rectenna enhances the harvested RF power with the minimization in the impedance matching requirement of the designed rectenna. A dual-band ambient energy harvester for on-body applications is reported in [21]. Another triangular-shape omnidirectional antenna with an input impedance of 100 Ω for rectifier impedance matching is presented in [22] for energy harvesting applications in the RF domain.

The upper bound of the rectifying diode resistance is defined by the input resistance of the nano-antenna which usually ranges from a few hundred to a few tens ohms [10,23]. The researchers have used various symmetric (Ni-NiO-Ni [24,25], polysilicon-SiO_2-polysilicon [26], Graphene-Air-Graphene [27]) and asymmetric (Ni-NiO-Pt [28], Ni-NiO-Cr/Au [29], polysilicon-SiO_2-Au [3], Al-AlO_x-Pt [30], Ni-NiO-Cu [31], Al-Al_2O_3-Pt [32], Cu-CuO-Au [7], Au- Al-Al_2O_3-Ti [5], Ti-TiO_2/ZnO-Al [23]) configurations of the MIM diode to achieve the matching resistance and high responsivity of the diode. It has been shown in [10,33] that tunneling didoes with a single layer of sandwiching oxide insulator did not produce high near zero-bias responsivity.

In this work, we design and analyze the performance of a double insulator-based (MIIM) rectenna for efficient energy harvesting applications in the IR region as illustrated in Fig. 1. The fabrications of the rectifying diode with multiple insulators exhibiting different electron affinities and bandgaps can produce high responsivity. Firstly, an optimized 28.3 THz resonant optical nano log-spiral antenna is designed (see Fig. 2) for the enhanced capturing of the incident IR radiations

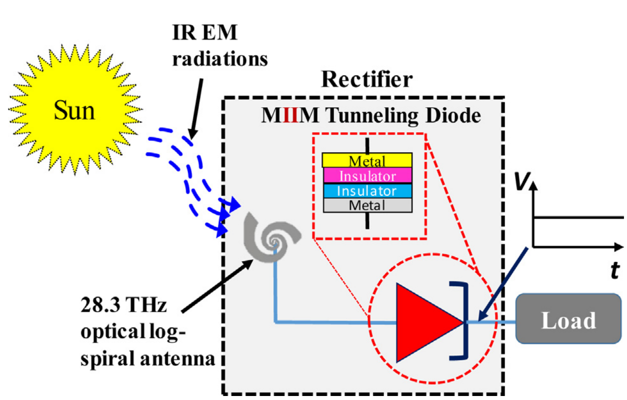

Fig. 1 Infrared (IR) rectenna system for energy harvesting using proposed MIIM based rectification.

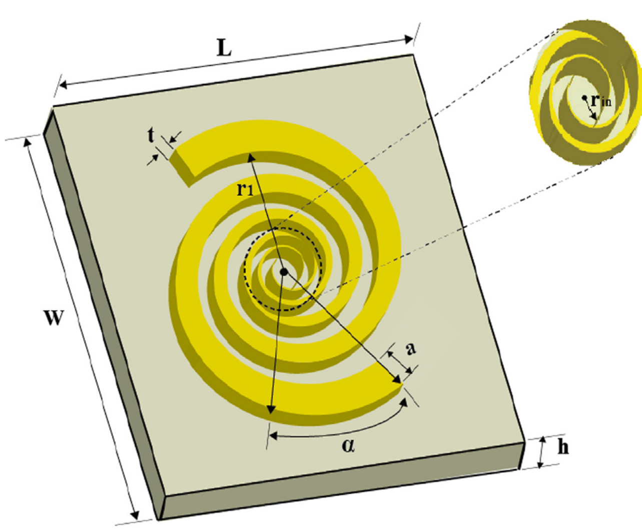

Fig. 2 Schematic of the designed log-spiral nano IR antenna; r_1: inner radius of the spiral, α: increment angle, *a*: growth rate, *t*: thickness of the conductor (gold) material, *L*: length of the substrate, *W*: width of the substrate, and *h*: thickness of the substrate.

as compared to earlier proposed designs [4,5,7,8,11–15]. To ensure the maximum transfer of received IR radiations by the antenna, we used a novel approach of creating the rectification part between the feeding terminals of the designed antenna as illustrated in Fig. 3. The realized log-spiral antenna arms act as the metallic terminals of diode electrodes while the two insulators are inserted between the metallic arms of the antenna. This configuration offers advantages of maximum conversion of the received IR waves by the antenna terminals along with high responsivity and low resistivity of the rectenna due to the localized transfer of the capturing EM radiations to the rectifying part. The study includes a detailed analysis of the effect of the metallic materials (Au, Al, Ag, and Cu as antenna arms) and ten combinations of the two sandwiching insulators to determine the suitable choice of the materials for the presented MIIM rectenna.

The rest of the manuscript is organized as follows. Section 2 details the design of the proposed rectenna. The performance analysis of the realized rectenna with different metals and insulators combinations is presented in Section 3. Section 4 includes the discussion while some conclusions of the presented study are drawn in Section 5.

2. Rectenna design

The proposed IR MIIM-based rectenna system is shown in Fig. 1. The schematic of the designed antenna is shown in Fig. 2. The geometric parameters of Fig. 2 antenna are optimized for the maximum electric field capturing around the two input terminals of the antenna which is referred to as the hotspot region. The log-spiral antenna structure is chosen due to its associated properties of circular polarization and wideband operation [34–36].

Table 1 lists the optimized design parameters of Fig. 1 for the maximum electric field enhancement characteristics. The quartz material having a relative permittivity of 3.78 and tan δ of 0.0001 is used as the substrate of the realized optical antenna. Due to surface plasmon polaritons, the behavior of metals is different at THz frequencies than radio frequency range. The classical Drude–Lorentz model (also known as the Drude model) is used for the modeling of the frequency-dependent conductivity and dispersion properties of the involved metals in the proposed rectenna. The Drude model helps us to accurately model the evaluations in the metal permittivity at the optical and terahertz range [4,7]. The full-wave EM analysis of the designed antenna is performed in HFSS in the frequency range of 27–30 THz.

Fig. 4 the reflection parameters of the nano-IR antenna of Fig. 2 only without insulators. The comparison of the S_{11} results shows that reflection characteristics of the realized

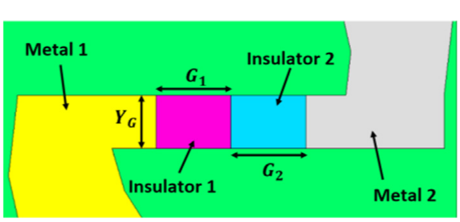

Fig. 3 Designed metal–insulator-insulator–metal (MIIM) configuration.

Table 1 Designed Nano-IR antenna parameters.

Parameter	Values(μm)
L (substrate length)	7.8
W (substrate width)	7.8
h (substrate thickness)	99.1
r_1 (inner radius of the spiral)	0.02
N (number of turns)	2.1
δ (spiral-patch width)	115
α (increment angle)	1.8°
a (growth rate)	0.31
t (spiral-patch thickness)	0.062

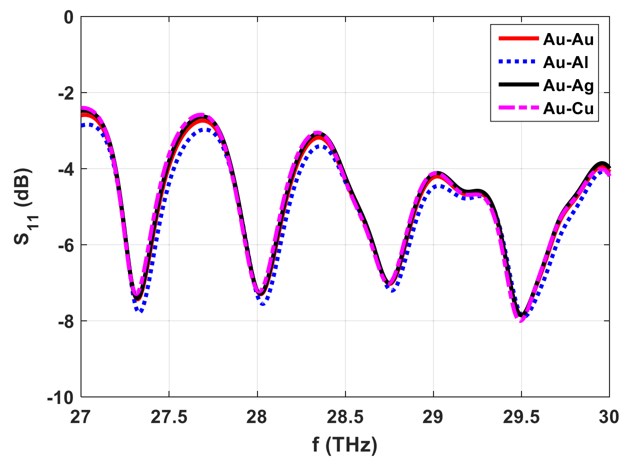

Fig. 4 Comparison of reflection parameters of the nano-antenna only without insulators.

nono-IR antenna are almost similar for all configurations of the conductor materials. Fig. 5 depicts the realized gain of the nano-antenna in the analyzed frequency range. As like S_{11} results, no variations in the gain of the antenna are noticed with the change in the materials of the IR-antenna arms. The far-field radiation pattern of the designed nano-antenna only

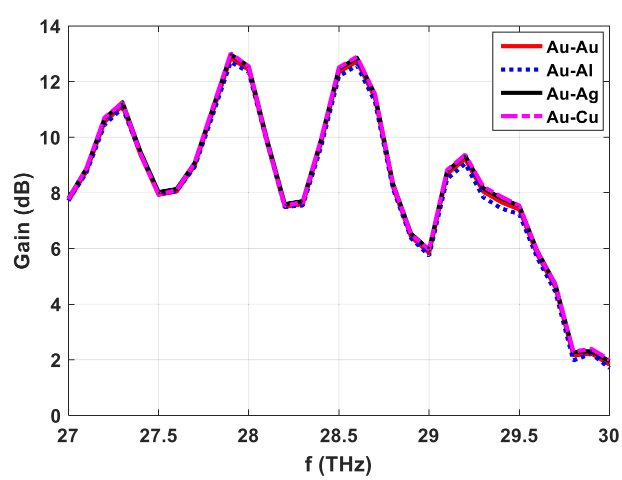

Fig. 5 Comparison of realized gain of the nano-antenna only without insulators.

are shown in Fig. 6. The radiation pattern results are shown only for two configurations of Au-Au and Au-Cu for brevity.

The captured solar energy by the optical antenna is forwarded to the rectification circuit for the conversion to the DC levels. The impedance matching between the antenna terminals and the rectifications circuit has a significant impact on the transfer efficiency of the captured IR radiations by the antenna. For the localized tunneling of the absorbed IR radiations by the optical antenna to ensure maximum conversion efficiency and non-linearity of the rectenna, two insulators are placed between the hotspot region of the antenna. Fig. 3 depicts the designed metal–insulator-insulator–metal (MIIM) configurations of the proposed rectenna. The variations in the bandgap and electron affinities of the two different oxide insulators can increase the non-linear characteristics of the rectifying diode [10,33]. The log-spiral antenna arms are used as the metallic electrodes of the rectifying MIIM diode while the two different oxide insulators are inserted between the metallic arms of the antenna. This novel employed approach offers the advantages of maximum conversion of the received IR waves by the antenna terminals. The immediate localized propagation of the received solar energy through the insulating materials junctions minimizes the losses and increased the rectifying output levels with a high near zero-bias responsivity of the realized rectenna.

The operation characteristics of the designed MIIM diode depend on metal properties, formation structure (symmetric or asymmetric), oxide insulator type and thickness, and operating frequency. The high sensitivity of the rectenna around zero-biased operation could be achieved by using different work function metals [3,23,26,30]. Such asymmetric configuration of the MIM diode increases the diode resistance and decreases the rectenna coupling efficiency. The coupling efficiency could be enhanced by employing the same metallic material in a diode structure as it minimizes the diode resis-

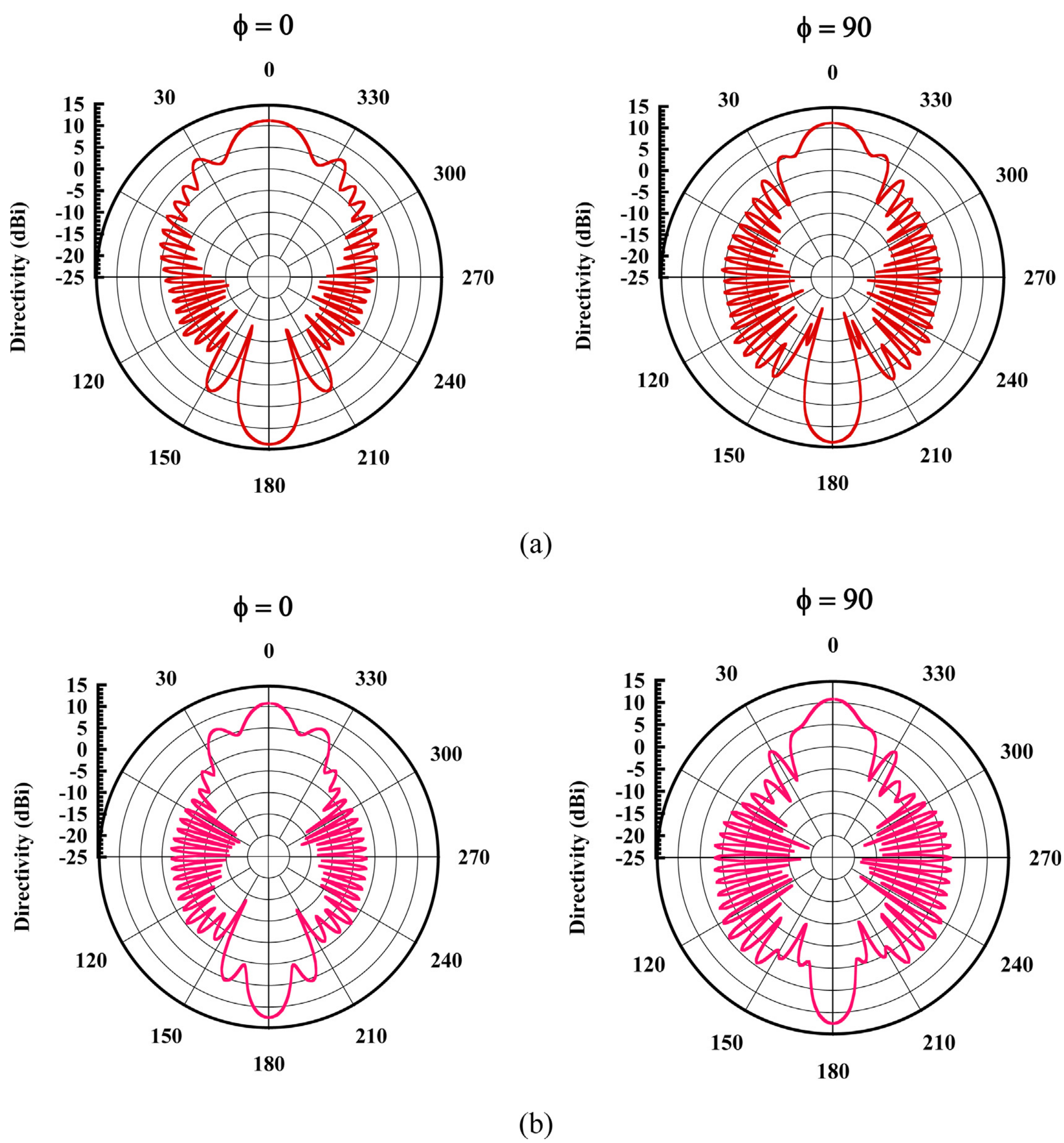

Fig. 6 Comparison of far-field radiation patterns of the nano-antenna only without insulators (a) configuration Au-Au; (b) configuration Au-Cu.

tance. However, it drastically impacts the near-zero bias operation of the diode [25,27].

A detailed parametric study was conducted for the determination of the optimized dimensions of the insulating materials. The obtained optimized values of the width (Y_G) and lengths (G_1 and G_2) of the insulators are 1 nm and 2 nm respectively. These dimensions remain fixed in the conducted study. The performance of the designed MIIM rectenna is analyzed by changing the material characteristics of the metals and insulators components of the rectenna with varying work functions. The gold material (Au) is chosen as metal 1 and it remains fixed for the whole analysis in this study.

The metal 2 on the other arm of the log-spiral rectenna (second electrode) is varied from Au to Al (aluminum) to Ag (silver) and to Cu (copper) to form both symmetric and asymmetric configurations of MIIM respectively. The work functions of Au, Ag, and Cu are 5.1 eV, 4.28 eV, 4.26 eV, and 4.53/5.1 eV respectively. Table 2 summarizes the work functions of the analyzed metals. Different combinations of the five oxide insulating materials (Al2O3, Cu2O, Ta2O5, TiO2, and ZnO) having different electron affinities (shown in Table 3) are analyzed for the characterization of the designed rectenna performance in terms of the electric field enhancement, current–voltage characteristics, resistance, and responsivity. The electron affinity of Al2O3, Cu2O, Ta2O5, TiO2, and ZnO are 2.58 [37], 3.2 eV [38], 3.2 eV [39], 3.9 eV [40], and 4.1 eV [40] respectively. Table 4 summarizes the ten different analyzed combinations of the proposed double insulator MIIM rectenna with the changes of the metallic material of the electrodes. and ZnO) having different electron affinities (shown in Table 3) are analyzed for the double insulator MIIM rectenna with the changes of the metallic material of the electrodes.

3. E-field characterization results

The characterization of the realized MIIM rectenna is performed as per the defined combinations of metallic electrodes and insulators in Table 4. The four analyzed combinations of electrodes metallic material are Au-I_1 I_2-Au, Au-I_1 I_2-Al, Au-I_1 I_2-Ag, and Au-I_1 I_2-Cu respectively. This section details the variations in the electric field, current/voltage, resistance, and responsivity of the investigated rectenna structure for the aforementioned metallic material combinations along with elaborated ten combinations of two insulators in Table 4. The full-wave characterization of the rectenna is performed for all insulators combinations of Table 4 for each formed metallic pair of MIIM rectenna.

Table 2 Work function of analyzed metals.

Metal	Work function (eV)	Work function difference (eV) with respect to Au
Gold (Au)	5.1	0
Aluminum (Al)	4.28	0.82
Silver (Ag)	4.26	0.84
Copper (Cu)	4.53	0.57

Table 3 Electron affinities of analyzed insulators.

Oxide Insulator	Electron affinity (eV)
Al2O3	2.58
Cu2O	3.2
Ta2O5	3.2
TiO2	3.9
ZnO	4.1

Table 4 Analyzed combinations of designed MIIM based rectenna (Italic values in () represents the work functions of metals and electron affinities of insulators in eV).

Metal 1	Insulator 1 (2 nm)	Insulator 2 (2 nm)	Metal 2
Au *(5.1)*	Al2O3 *(2.58)*	Cu2O *(3.2)*	**Au *(5.1)* /Al *(4.28)* /Ag *(4.26)* /Cu *(4.53)***
	Al2O3 *(2.58)*	Ta2O5 *(3.2)*	
	Al2O3 *(2.58)*	TiO2 *(3.9)*	
	Al2O3 *(2.58)*	ZnO *(4.1)*	
	Ta2O5 *(3.2)*	Cu2O *(3.2)*	
	Ta2O5 *(3.2)*	TiO2 *(3.9)*	
	Ta2O5 *(3.2)*	ZnO *(4.1)*	
	TiO2 *(3.9)*	Cu2O *(3.2)*	
	TiO2 *(3.9)*	ZnO *(4.1)*	
	Cu2O *(3.2)*	ZnO *(4.1)*	

Fig. 7 shows the captured electric field variations across the antenna (electrode) terminals for the Au-I_1 I_2-Au MIIM configuration. The two insulators (I_1 and I_2) are changed as per the 10 mentioned combinations in Table 4 and electric field results are recorded for each combination. We note from Fig. 7 that for this symmetric MIIM (Au-I_1 I_2-Au) configuration, the maximum induced E-field levels are obtained for the Au-Al2O3-Cu2O-Au formation of the insulating materials

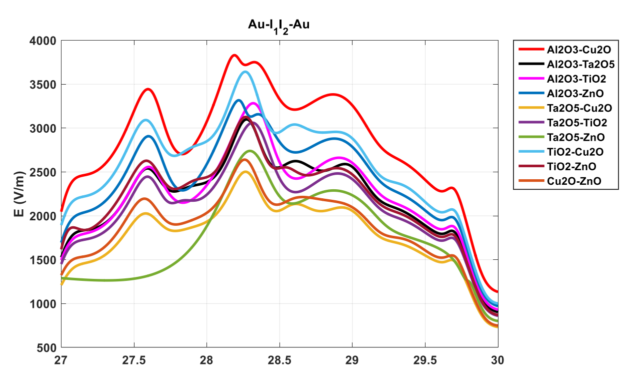

Fig. 7 Comparison of induced E-field variations with the change in double insulators combinations for Au-I1 I2-Au MIIM formation.

(more than 3500 V/m at 28.3 THz). The induced electric field in the gap region of the antenna reduces as we moved to the other 9 combinations of the insulators for this symmetric MIIM case, as depicted in Fig. 7. The least levels of induced E-field are observed when the two insulators are changed to Ta2O5-Cu2O.

The next analyzed configuration for the induced electric field variations across the antenna gap terminals is asymmetric. In this configuration, the material of the second arm of the antenna (electrode) is changed to Al to construct Au-I_1 I_2-Al MIIM formation. The analysis of the E-field for this formation is illustrated in Fig. 8. The results reflect that among the analyzed combinations of insulators, the best and worst candidates of captured E-field enhancement at the antenna terminals are Al2O3-Cu2O and Ta2O5-Cu2O respectively. The MIIM rectenna formation of Au-Al2O3-Cu2O-Al (red curve in Fig. 8) produces the maximum E-field levels in the entire analyzed frequency band with a maximum value of around 4000 V/m at 28.3 THz. We can observe that the combination of Au-Ta2O5- Cu2O -Al reduces the induced E-fields levels to minimum values as compared to all other combinations.

The next asymmetric MIIM formation involves the change of the second electrode material to silver while keeping the gold as the first electrode material. Fig. 9 presents the variations in the induced E-field levels across the log-spiral antenna electrodes for the 10 combinations of the double insulating materials of Table 4. As like first symmetric (Au-I_1 I_2-Au) and asymmetric (Au-I_1 I_2-Al) formations, this asymmetric configuration of Au-I_1 I_2-Ag produces the maximum induced E-fields when Al2O3 and Cu2O are chosen as the double insulating options of the designed MIIM rectenna. It can be noted from Fig. 9 that the maximum level of the captured E-field by the antenna terminals for Au- Al2O3-Cu2O –Ag formation is more than 4000 V/m.

As the earlier discussed symmetric and asymmetric MIIM arrangements, a similar trend of E-field variations is observed for the third analyzed asymmetric MIIM formation of Au-I_1 I_2-Cu with the change of second electrode material to copper. The results for this formation are shown in Fig. 10. We can note that the worst combination referring to the minimum level of induced E-field is Au-Ta2O5- Cu2O–Cu formation of metals and insulators. On the contrary, as for the aforementioned analyzed configurations, the addition of Al2O3 and Cu2O as the insulators between the antenna terminals results in the maximum capturing (more than 4000 V/m around 28.3 THz) of the illuminating E-field by the designed log-spiral antenna electrodes.

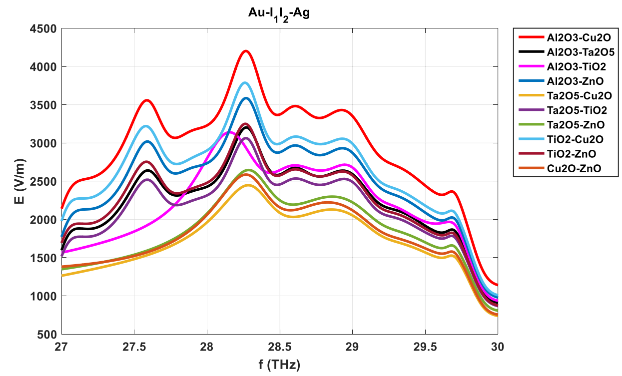

Fig. 9 Comparison of induced E-field variations with the change in double insulators combinations for Au-I1 I2-Ag MIIM formation.

The electric field analysis of Figs. 7–10 deduces that using different metallic materials as the diode electrodes *i.e.* asymmetric formation produces enhanced levels of induced E-field as compared to the symmetric analyzed arrangement of Au-I_1 I_2-Au.

4. Rectification characterization results

4.1. Basics of rectification performance characterization

The rectification performance of the MIIM is characterized in terms of current–voltage, resistivity, and responsivity properties [23]. Equation (1) is used for the determination of the small-signal resistance of the realzied MIIM [41]. In (1) I_1' represents the first derivate of the average (DC) current with respect to the biasing voltage.

$$R = \frac{1}{I'} \quad (1)$$

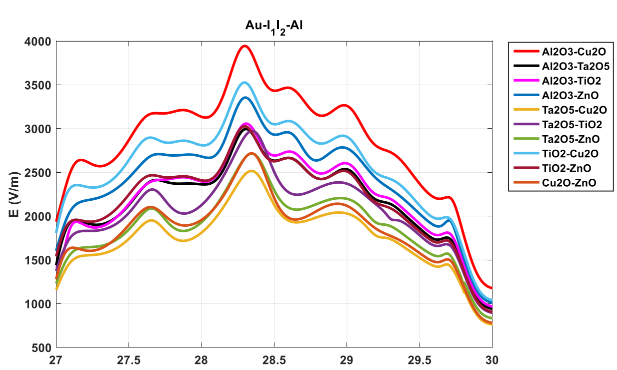

Fig. 8 Comparison of induced E-field variations with the change in double insulators combinations for Au-I1 I2-Al MIIM formation.

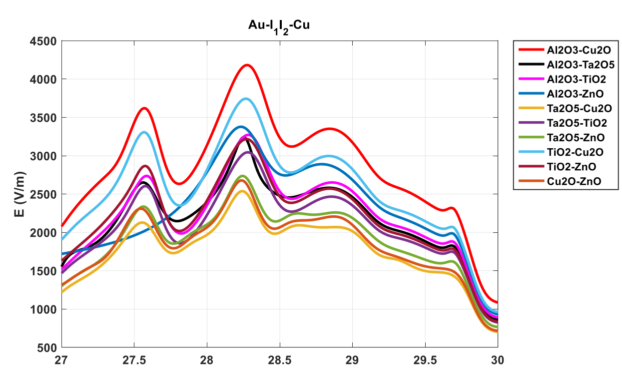

Fig. 10 Comparison of induced E-field variations with the change in double insulators combinations for Au-I1 I2-Cu MIIM formation.

Responsivity (S) of a rectifier is computed to investigate its non-linear operation. It is commonly estimated by the ratio of the second and first derivates of direct current (DC) with respect to voltage as shown in (2) [41]. It is used to determine the rectified DC output current per watt characteristics of the analyzed MIIM rectifier.

$$S = \frac{I''}{2I'} \quad (2)$$

A sinusoidal signal with radiation frequency of ω and amplitude of V is added to the DC bias voltage (V_B) of the rectifier for the modeling of the illuminating IR radiations. The net voltage across the MIIM's terminal (V_{MIIM}) is represented using (3)

$$V_{MIIM} = V_B + V cos(\omega t) \quad (3)$$

The product of AC signal angular frequency ω and $\hbar$(reduced Plank's constant) gives us the energy of the incident photons *i.e.* $E_p = \hbar\omega$. The zapping of the MIIM rectifier with ultra-high IR radiations brings the difference among the photons energy levels to E_p from the previous energy levels of E. As investigated in [42], the photon energy (E_p) can be used for the the estimation of R and S using (4) and (5). E represents the electrong charge in (4) and (5).

$$R = \frac{2\hbar\omega}{e} \frac{1}{I\left(\frac{\hbar\omega}{e}\right) - I\left(-\frac{\hbar\omega}{e}\right)} \quad (4)$$

$$S = \frac{e}{\hbar\omega} \frac{I\left(\frac{\hbar\omega}{e}\right) + I\left(-\frac{\hbar\omega}{e}\right)}{I\left(\frac{\hbar\omega}{e}\right) - I\left(-\frac{\hbar\omega}{e}\right)} \quad (5)$$

The tunneling current ($I(V)$) of the MIIM diode at its biasing voltage V_B is calculauted using (6) [10,23,43]

$$I(V_B) = \frac{4\pi m_e}{h^3} \int_0^\infty T(E_\infty) \times \int_0^{E_\infty} [f_L(E) - f_R(E + eV_B)] dE dE_\infty \times A \quad (6)$$

In (6), h depicts the Plank's constant, m_e represents the effective mass of the electron, f_L and f_R are left and right electron current distributions of the corresponding sides of the realized MIIM. These current distributions are computed using the Fermi-Dirac function. The transmission probability of the electron to tunnel through the barrier with an energy E is represented using $T(E)$. $T(E)$ is computed using the transfer matrix method (TMM) by employing an airy function as detailed in [44]. Lastly, A is representing the quantum tunneling placing area between the metals and insualtros of the MIIM. The perfformacne characterization of the recitfication properties of the realized MIIM structures is done using (1)-(6) and is detailed in the following sections.

4.2. Current-Voltage (I-V) characteristics

The characterization of the current–voltage variations for the different analyzed combinations of metals and insulators from Table 4 is discussed here.

Fig. 11 compares the changes in the current density of the symmetric arrangement of the MIIM diode with both electrode materials as gold. The variations in the current density are analyzed by varying the bias voltage between −2 V to +2 V. Note that to see the variation of all the curves we present the current density (J) in the logarithmic scale *i.e.* log10 (J). It can be observed from Fig. 11 that the best results of I/V variations are obtained for the case when the Al2O3 and Cu2O are chosen as the insulating material of the MIIM diode. The next better performance is for the insulator combinations of Al2O3 and Ta2O5. The change of the double insulator's combination to TiO2-ZnO produces the worst I/V characteristics for the symmetric analyzed MIIM arrangement.

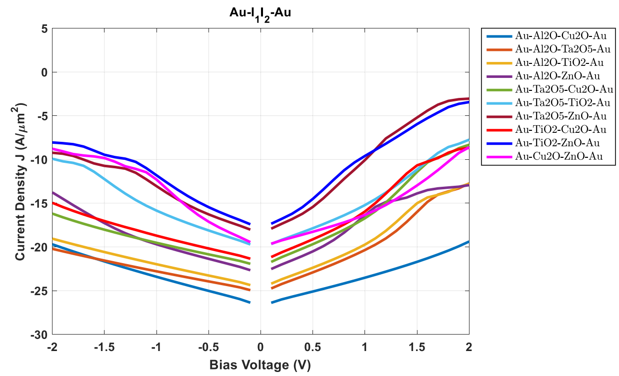

Fig. 11 Comparison of induced current density with the change in double insulators combinations for Au-I1 I2-Au MIIM formation.

The first asymmetric analyzed case of the MIIM configuration to observe the changes in current–voltage characteristics of the designed MIIM diode is Au-I_1 I_2-Al. In this asymmetric formation, the second electrode materials are changed to aluminum. The comparison of the I/V characteristics for the ten combinations of Table 4 insulators are depicted in Fig. 12. The results show that the MIIM formation of Au- Al2O3-Cu2O –Al produces superior results as compared to all other insulator changes. Similar observations of the variations in the current density symmetry with the changes in the bias voltage can be made in Figs. 13 and 14 respectively. Figs. 13 and 14 illustrate the I/V characteristics of the other two analyzed asymmetric configurations of MIIM diode *i.e.* Au-I_1 I_2-Ag and Au-I_1 I_2-Cu. The maximum value of the current density for the symmetric (Au-I1 I2-Au) and asymmetric (Au-I_1 I_2-Al, Au-I_1 I_2-Ag, and Au-I_1 I_2-Cu) cases of Figs. 11-14 is 4.61 E-20 A/μm^2, 4.80 E−16 A/μm^2, 4.80 E−16 A/μm^2, and 7.71 E−17 A/μm^2 respectively for the +2 V bias voltage. The overall characteristics of Figs. 11-12 are exhibit symmetric behavior in the range of −0.5 V to 0.5 V biasing voltage range.

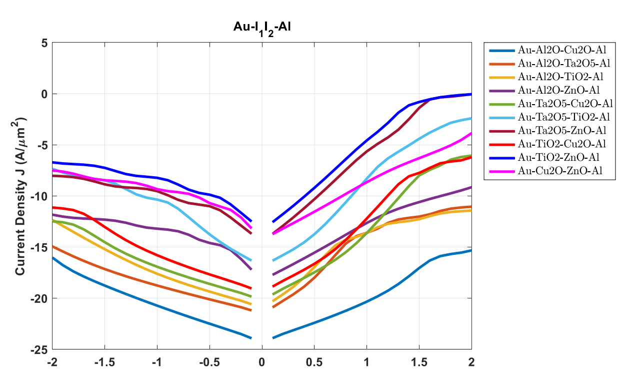

Fig. 12 Comparison of induced current density with the change in double insulators combinations for Au-I1 I2-Al MIIM formation.

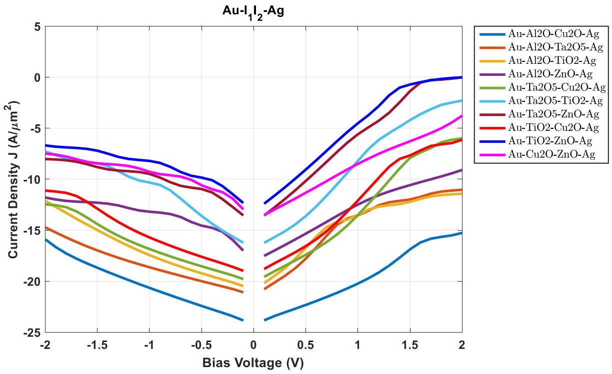

Fig. 13 Comparison of induced current density with the change in double insulators combinations for Au-I1 I2-Ag MIIM formation.

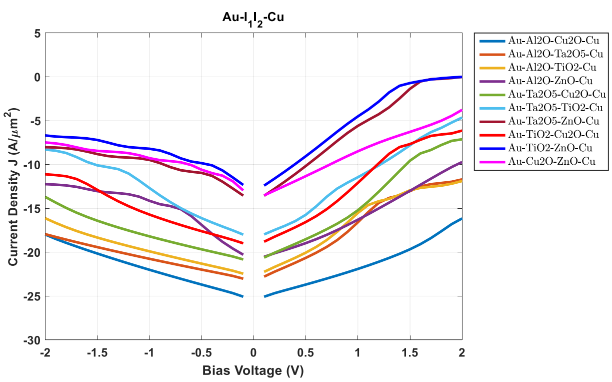

Fig. 14 Comparison of induced current density with the change in double insulators combinations for Au-I1 I2-Cu MIIM formation.

4.3. *Resistance characteristics*

The near-zero bias resistance of the designed rectifying diode significantly impacts the performance of the rectenna system. Fig. 15 compares the resistance curves for the symmetric structure of the MIIM diode with both electrode metals as the gold material. Note to see the variation of all the curves we present the resistance (R) results in logarithmic scale *i.e.* log10(R). It can be observed from Fig. 15 that the maximum resistance value (2.45E + 25 Ω. µm^2) at zero-bias voltage is noted for the Au- Al2O3-Cu2O –Au MIIM structure. The resistance value decreases with the change in insulators to Al2O3-Ta2O5, Al2O3-TiO2, and so on. The formation of TiO2 and ZnO produces the least value of the resistance around 0 V bias voltage as illustrated in Fig. 15.

The asymmetric arrangement of the designed MIIM rectenna produces the lower values of the near zero-bias voltage resistance as illustrated in Figs. 16-18. The Au-Al2O3-Cu2O -Al formation of MIIM rectenna lowers the maximum resistance value to 8.10E + 22 Ω. µm^2 @ −0.1 V as compared to the symmetric formation of Au-Al2O3-Cu2O –Au. The change of metallic electrodes to Au and Ag did not bring a change in the maximum value of the recorded resistance value for the perfect combination of Al2O3 and Cu2O as the insulating materials as illustrated in Fig. 17. The maxim observed value for this case is also 8.10E + 22 Ω. µm^2 @ −0.1 V for the Au-Al2O3-Cu2O –Ag MIIM configuration. The comparison of curves in Fig. 18 for the asymmetric arrangement of Au-I_1 I_2-Cu shows that the maximum zero-bias voltage resistance, in this case, is 1.18E + 24 Ω. µm^2 when Al2O3 and Cu2O are used as the insulating material of double insulator MIIM con-

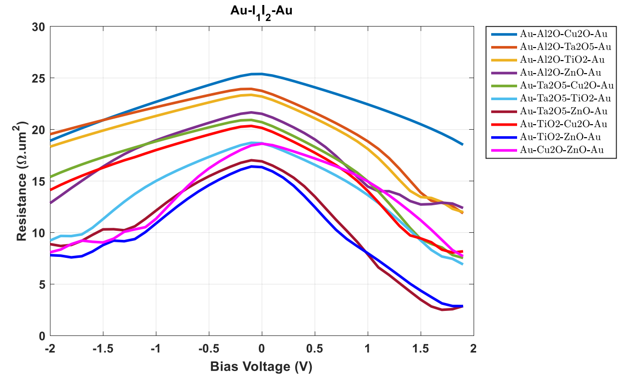

Fig. 15 Comparison of variations in resistance with the change in double insulators combinations for Au-I1 I2-Au MIIM formation.

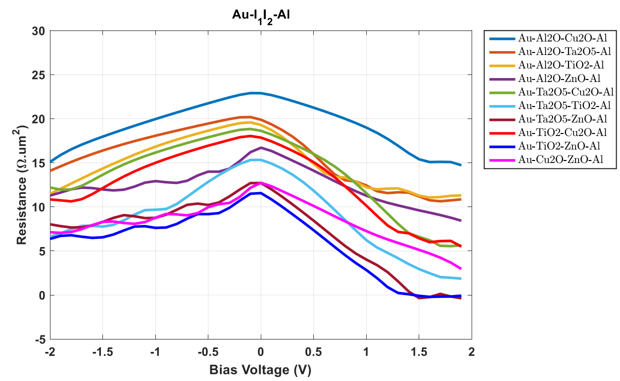

Fig. 16 Comparison of variations in resistance with the change in double insulators combinations for Au-I1 I2-Al MIIM formation.

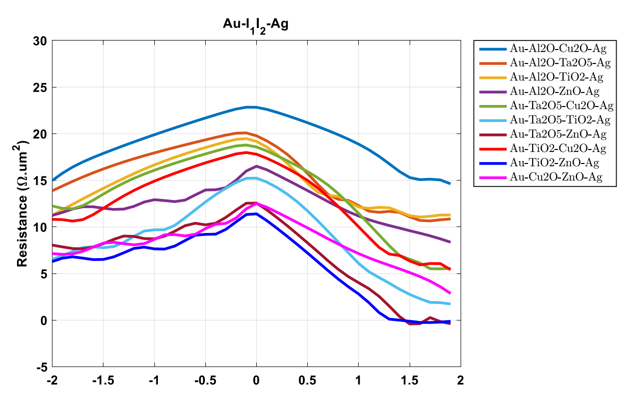

Fig. 17 Comparison of variations in resistance with the change in double insulators combinations for Au-I1 I2-Ag MIIM formation.

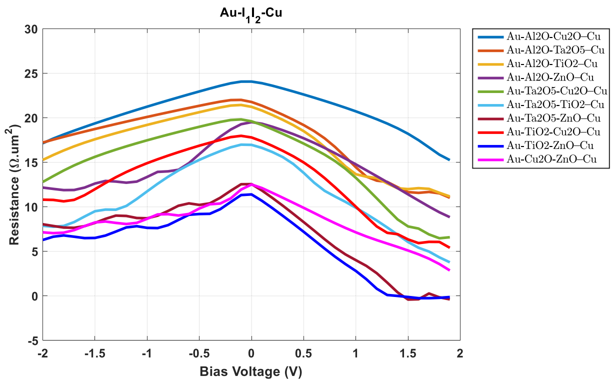

Fig. 18 Comparison of variations in resistance with the change in double insulators combinations for Au-I1 I2-Cu MIIM formation.

figuration. The change of the second electrode metal to copper increase the maximum near zero-bias resistance value as compared to silver and aluminum metals. However, this value is lower than the observed maximum resistance value for the MIIM symmetric formation of Au-Al2O3-Cu2O –Au.

4.4. Responsivity characteristics

Responsivity is the ratio of the output DC and input AC power at the terminals of the diode. High responsivity is essential for the high-efficiency rectenna system.

The variations in the responsivity of the designed MIIM rectenna system with the changing insulator characteristics of the Au-I_1 I_2-Au MIIM formation are depicted in Fig. 19. Note that to see the variation of all the curves we present the responsivity (S) results in logarithmic scale of log10(S). The analysis reflects that the maximum responsivity value of 4.69 A/W @ 1.3 V is recorded for the insulator's combinations of Cu2O and ZnO. The worst responsivity response is noted for the Au-Al2O3-Cu2O –Au MIIM configuration. For this case, the maximum value of responsivity is 3.65 A/W for the biasing voltage of 1.8 V. It can also be noted that for the positive biasing voltage range of 0 – 2 V, the relative maximum value of the responsivity has fewer variations with the change in the insulators type as compared to the resistance properties of the same MIIM configuration.

Figs. 20, 21 and 22 compare the responsivity curves for the asymmetric formations (Au-I_1-I_2-Al, Au-I_1 I_2-Ag, and Au-I_1 I_2-Cu) of the MIIM rectenna. The asymmetric formation of the MIIM rectenna with different work function metals increases the overall non-linear characteristics of the rectenna system as can be noted by comparing the Figs. 20-22 curves with Fig. 19 curves

5. Discussion

The presented detailed analysis in the last section confirms that the variations of the work functions of the electrode's metals and electron affinities of the insulators changes the bandgap barrier heights of each MIIM formation and thus significantly impact the absorbed electric field in hotspot region, I/V, resistance and responsivity characteristics of the realized MIIM structure.

The summary of performance characterization of analyzed symmetric and asymmetric arrangements of MIIM rectenna in the last sections is presented in Tables 5–8 respectively. Please note that all the summarized characterization values in Tables 5–8 are in linear scale for the symmetric comparison. These tables present the captured E-field values at 28.3 THz, the maximum value of current density, resistance, and responsivity in the analyzed biasing voltage range of -2 to $+2$ V.

We can note from Table 5 that the maximum value of captured E-field across electrodes terminals, resistance and current density, and the minimum value of responsivity are observed for the Au-Al2O3-Cu2O –Au arrangement. It is because of the maximum absolute barrier height of 2.52 eV and 1.9 eV for the Au/ Al2O3 and Cu2O/Au tunneling junctions respectively. This absolute barrier height changes to 1.9 eV, 1.2 eV, and 1 eV with the change in the second insulator to Ta2O5, TiO2, and ZnO in the realized symmetric MIIM formation of Au-Al2O3-I_2 –Au. The reduction of this barrier height lowers the maximum induced E-field at 28.3 THz, resistance, and current density values while increasing the responsivity around the zero-bias voltage. Owing to the smallest barrier height of 1.9 eV, 1 eV for the Au/ Al2O3, and Cu2O/Au tunneling junctions, the lowest values of performance parameters are recorded for the Au-Cu2O-ZnO –Au MIIM formation.

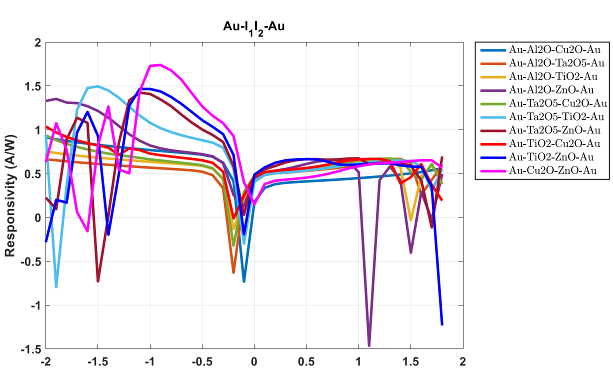

Fig. 19 Comparison of variations in responsivity with the change in double insulators combinations for Au-I1 I2-Au MIIM formation.

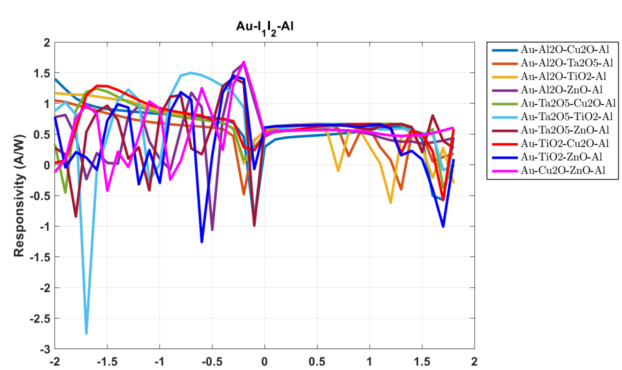

Fig. 20 Comparison of variations in responsivity with the change in double insulators combinations for Au-I1 I2-Al MIIM formation.

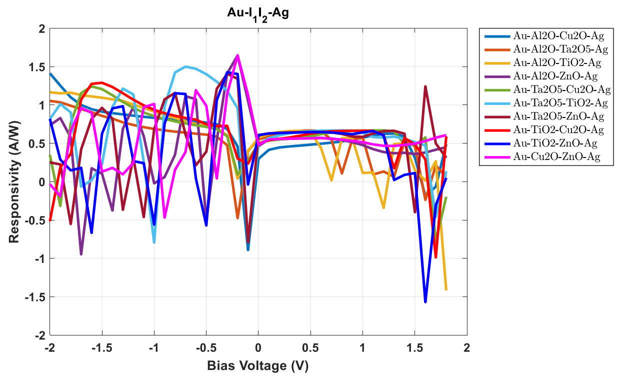

Fig. 21 Comparison of variations in responsivity with the change in double insulators combinations for Au-I1 I2-Ag MIIM formation.

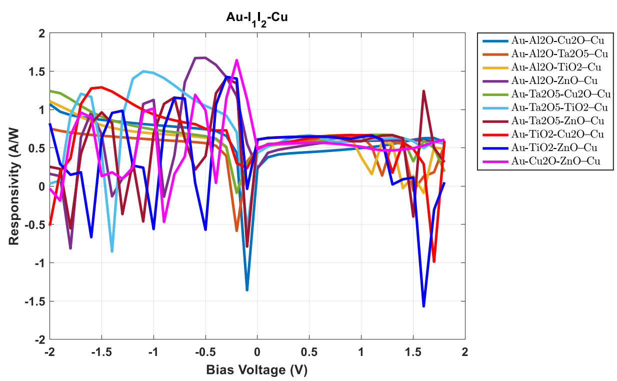

Fig. 22 Comparison of variations in responsivity with the change in double insulators combinations for Au-I1 I2-Cu MIIM formation.

The change of the second electrode metal to aluminum (Al) changes the barrier height of the second (insulator/ Al metal) tunneling junction to 1.08 eV, 1.08 eV, 0.38 eV, 0.18 eV for the Cu2O, Ta2O5, TiO2, and ZnO insulators in the MIIM configuration Au-Al2O3-I_2 –Al. Also, the difference between the work function values of the two electrode metals is 0.82 eV in this case (see Table 2). The decrease in the barrier heights and metalwork function's differences enhances the captured E-fields level by the factor of 202 V/m, −70 V/m, 191 V/m, and 224 V/m as compared to the corresponding symmetric configurations of Au-Al2O3- Cu2O –Au, Au-Al2O3- Ta2O5 –Au, Au-Al2O3- TiO2 –Au, and Au-Al2O3- ZnO –Au respectively. A similar observation can be made by comparing the Tables 7 and 8 results with Table 5 values. The comparison shows that overall decrease in barrier heights due to variations in the electrodes and insulators material types by using low work function metal as the second electrode in the asymmetric formations produce better performance in terms of enhanced resonant 28.3 THz E-field, maximum values of resistance, current density and non-linearity of the proposed MIIM rectenna system. The overall best performance is obtained for the MIIM formation of Au-Al2O3- Cu2O –Cu. The obtained results show that this configuration (Au-Al2O3- Cu2O –Cu) could be used for the optimal performance of the proposed rectenna system for energy harvesting applications with maximum levels of absorbing solar energy and appropriate values of the resistance and responsivity of the system to ensure conversion efficiency.

Table 9 lists the performance characteristics of the single insulator-based (MIM) rectenna system of the same proposed configuration of Fig. 3 with the removal of the second installed insulator. The performance comparison of the proposed double insulator-based rectenna system (MIIM) with a single insulator-based (MIM) rectenna system reflects that the overall non-linear characteristics (responsivity) of the MIIM rectenna systems are improved by a factor of 2 as compared to a single insulator based rectenna system.

Table 5 Summary of performance characterization of Au-I1I2 –Au MIIM configuration.

Au-I1I2-Au					
Insulator 1 (2 nm)	**Insulator 2(2 nm)**	**E Field at28.3 THz(V/m)**	**Max J(A/μm2)**	**Max R(Ω.μm2)**	**Max S(A/W)**
Al2O3	Cu2O	3741	4.16E-20 @ 2 V	2.45E + 25 @ 0 V	3.65 @1.8 V
Al2O3	Ta2O5	3065	1.82E-13 @ 2 V	8.78E + 23 @ −0.1 V	4.65 @ 1.3 V
Al2O3	TiO2	3274	1.70E-13 @ 2 V	2.32E + 23 @ −0.1 V	4.60 @ 1.2 V
Al2O3	ZnO	3130	1.17E-13 @ 2 V	4.61 + 21 @ −0.1 V	4.53 @ 0.8 V
Ta2O5	Cu2O	2462	1.82E-08 @ 2 V	5.23E + 18 @ −0.1 V	4.45 @ 1.4 V
Ta2O5	TiO2	3056	8.93E-04 @ 2 V	1.05E + 17 @ −0.1 V	4.72 @ 1 V
Ta2O5	ZnO	2738	2.11E-09 @ 2 V	2.24E + 20 @ −0.1 V	4.64 @ 1.1 V
TiO2	Cu2O	3576	3.63E-04 @ 2 V	2.59E + 16 @ −0.1 V	4.62 @ 0.5 V
TiO2	ZnO	3078	2.47E-09 @ 2 V	4.28E + 18 @ 0 V	4.48 @ 1.7 V
Cu2O	ZnO	2578	4.80E-09 @ 2 V	8.52E + 20 @ −0.1 V	4.69 @1.3 V

Table 6 Summary of performance characterization of Au-I1I2 –Al MIIM configuration.

Au-I1I2-Al					
Insulator 1 (2 nm)	**Insulator 2 (2 nm)**	**E Field at 28.3 THz (V/m)**	**Max J (A/μm^2)**	**Max R (Ω μm^2)**	**Max S (A/W)**
Al2O3	Cu2O	3943	4.80E-16 @ 2 V	8.10E + 22 @ –0.1 V	4.26 @ 1.3 V
Al2O3	Ta2O5	2995	8.95E-12 @ 2 V	1.55E + 20 @ –0.1 V	4.66 @ 0.5 V
Al2O3	TiO2	3056	3.76E-12 @ 2 V	3.85E + 19 @ –0.1 V	4.61 @ 0.4 V
Al2O3	ZnO	3354	7.21E-10 @ 2 V	5.15E + 16 @ 0 V	3.75 @ 0.6 V
Ta2O5	Cu2O	2482	0.003917 @ 2 V	2.14E + 15 @ 0 V	4.65 @ 0.8 V
Ta2O5	TiO2	2920	0.896464 @ 2 V	5.08E + 12 @ 0 V	4.63 @ 1.3 V
Ta2O5	ZnO	2672	6.23E-07 @ 2 V	1.10E + 18 @ –0.1 V	4.62 @ 1 V
TiO2	Cu2O	3524	0.86065 @ 2 V	3.65E + 11 @ 0 V	4.52 @ 1.1 V
TiO2	ZnO	3025	0.00014 @ 2 V	5.41E + 12 @ 0 V	4.04 @ 1.8 V
Cu2O	ZnO	2671	8.79E-07 @ 2 V	6.90E + 18 @ –0.1 V	4.66 @ 1.2 V

Table 7 Summary of performance characterization of Au-I1I2 –Ag MIIM configuration.

Au-I1I2-Ag					
Insulator 1 (2 nm)	**Insulator 2 (2 nm)**	**E Field at 28.3 THz (V/m)**	**Max J (A.μm$_2$)**	**Max R (Ω μm^2)**	**Max S (A/W)**
Al2O3	Cu2O	4131	5.53E-16 @ 2 V	6.96E + 22 @ –0.1 V	4.25 @ 1.3 V
Al2O3	Ta2O5	3157	9.24E-12 @ 2 V	1.21E + 20 @ –0.1 V	4.66 @ 0.5 V
Al2O3	TiO2	2832	9.24E-12 @ 2 V	1.21E + 20 @ –0.1 V	4.66 @ 0.5 V
Al2O3	ZnO	3529	8.13E-10 @ 2 V	3.26E + 16 @ 0 V	3.72 @ 0.6 V
Ta2O5	Cu2O	2441	0.005142 @ 2 V	1.70E + 15 @ 0 V	4.65 @ 0.8 V
Ta2O5	TiO2	3007	0.976206 @ 2 V	3.6E + 12 @ 0 V	4.60 @ 1.3 V
Ta2O5	ZnO	2641	7.44E-07 @ 2 V	9.56E + 17 @ –0.1 V	4.61 @ 1 V
TiO2	Cu2O	3693	0.980103 @ 2 V	2.52E + 11 @ 0 V	4.57 @ 1.1 V
TiO2	ZnO	3179	0.000174 @ 2 V	3.29E + 12 @ 0 V	4.04 @ 1.8
Cu2O	ZnO	2566	1.02E-06 @ 2 V	6.07E + 18 @ –0.1 V	4.66 @ 1.2 V

The employed design strategies for the identification of the suitable configurations of MIIM rectenna structures make it suitable for various practical applications of IR energy harvesting. The finding of a suitable design of the proposed rectenna with the identification of metal and oxide dimensions as per fabrication constraints, type of appropriate insulators, and compatibility of structure with e-beam or optical lithography favors the presented approach from the practical manufacturing point of view. The array configuration of the rectenna could also be designed and manufactured for the enhancement of the rectenna performance in terms of higher conversions efficiency.

6. Conclusions

This study has presented a comprehensive detailed analysis of the double insulator-based (MIIM) optical rectenna system for the harvesting of more than 50% untapped solar radiation at 28.3 THz. The novel design of the proposed rectenna system involves the usage of the resonant log-spiral antenna arms as the diode electrodes and the insertion of the two insulators in between them. The performed analysis with the variations in the metals of the electrodes (Au/Al/Ag/Cu) and ten different combinations of inserted five insulators (Al2O3, Cu2O,

Table 8 Summary of performance characterization of Au-I1I2 –Cu MIIM configuration.

Au-I1I2-Cu					
Insulator 1 (2 nm)	**Insulator 2 (2 nm)**	**E Field at 28.3 THz (V/m)**	**Max J (A/μm^2)**	**Max R (Ω.μm^2)**	**Max S (A/W)**
Al2O3	Cu2O	4159	7.17E-17 @ 2 V	1.18E + 24 @ 0 V	4.24 @ 1.7 V
Al2O3	Ta2O5	3060	2.03E-12 @ 2 V	1.04E + 22 @ −0.1 V	4.66 @ 0.9 V
Al2O3	TiO2	3261	1.32E-12 @ 2 V	2.79E + 21 @ −0.1 V	4.61 @ 0.8 V
Al2O3	ZnO	3282	1.94E-10 @ 2 V	3.30E + 19 @ 0 V	3.99 @ 1.4 V
Ta2O5	Cu2O	2422	2.29E-05 @ 2 V	9.78E + 16 @ −0.1 V	4.60 @ 0.5 V
Ta2O5	TiO2	3032	0.976206 @ 2 V	3.6E + 12 @ 0 V	4.60 @ 1.3 V
Ta2O5	ZnO	2619	7.44E-07 @ 2 V	9.56E + 17 @ −0.1 V	4.61 @ 1 V
TiO2	Cu2O	3707	0.980103 @ 2 V	2.52E + 11 @ 0 V	4.57 @ 1.1 V
TiO2	ZnO	3193	0.000174 @ 2 V	3.29E + 12 @ 0 V	4.04 @ 1.8 V
Cu2O	ZnO	2525	7.57E-08 @ 2 V	6.65E + 19 @ −0.1 V	4.68 @ 1.2 V

Table 9 Maximum resistivity (R) and responsivity (S) for the different metals of the MIM-diode.

At 28.3 THz		
Configuration	**Max *R* ($\times 10^{12}$ Ω μm^2)**	**Max *S* (A/W)**
Au-Al2O3-Au	1.47 @ −0.1 V	1.85 @ 2 V
Au-Al2O3-Al	1.36 @ −0.2 V	2.19 @ 2 V
Au-Al2O3-Ag	1.28 @ −0.25 V	2.2 @ 2 V
Au-Al2O3-Cu	4 @ −0.15 V	2.01 @ 2 V

Ta2O5, TiO2, and ZnO) deduces that asymmetric configuration with a larger difference in the work function of metals and lower barrier heights with insulators performs better in terms of absorbing E-field, I/V, resistance and responsivity characteristics. The non-linear characteristics of the investigated MIIM rectenna systems show 100% enhancement as compared to the same metals and insulator-based MIM rectenna.

The future work includes (i) fabrication and experimental measurements of the realized rectennas for different configurations; (ii) analysis of array configurations of the designed rectennas for the enhanced power efficiency; and (iii) analysis of the rectification performance of proposed MIIM structures with the computations of the rectified DC output through co-simulation and experimental measurements.

Declaration of Competing Interest

The authors declare that they have no known competing financial interests or personal relationships that could have appeared to influence the work reported in this paper.

Acknowledgments

The authors acknowledge the support provided by King Abdullah City for Atomic and Renewable Energy (K.A. CARE) under KA.CARE-King Abdulaziz University Collaboration Program. The authors are also thankful to Deanship of Scientific Research, King Abdulaziz University for providing financial support vide grant number (FP-068-43).

References

[1] M.B.M. Mokhar, S.R. Kasjoo, N.J. Juhari, N.F. Zakaria, An overview of semiconductor rectifier operating in the millimeter wave and terahertz region, AIP Conf. Proc. 2203 (1) (2020), p. 020039.

[2] L. Mescia, A. Massaro, New Trends in Energy Harvesting from Earth Long-Wave Infrared Emission, Advances in Materials Science and Engineering, vol. 2014, p. 252879, 2014/08/11 2014.

[3] M. Dagenais, K. Choi, F. Yesilkoy, A.N. Chryssis, M.C. Peckerar, Solar spectrum rectification using nano-antennas and tunneling diodes, in: Optoelectronic Integrated Circuits XII, 2010, vol. 7605, p. 76050E: International Society for Optics and Photonics.

[4] W. Amara, D. Oueslati, N. Eltresy, A. Alghamdi, K. Sedraoui, T. Aguili, H. Rmili, R. Mittra, Parametric study of modified dipole nano-antennas printed on thick substrates for infrared energy harvesting, Int. J. Numer. Model. Electron. Networks Devices Fields 33 (2) (2020), https://doi.org/10.1002/jnm.v33.210.1002/jnm.2704.

[5] G. Jayaswal, A. Belkadi, A. Meredov, B. Pelz, G. Moddel, A. Shamim, Optical rectification through an Al_2O_3 based MIM passive rectenna at 28.3 THz, Mater. Today Energy 7 (2018) 1–9.

[6] S. Joshi, G. Moddel, Simple figure of merit for diodes in optical rectennas, IEEE J. Photovoltaics 6 (3) (2016) 668–672.

[7] M.N. Gadalla, M. Abdel-Rahman, A. Shamim, Design, optimization and fabrication of a 28.3 THz nano-rectenna for infrared detection and rectification, Sci. Rep. 4 (1) (2014) 4270.

[8] T. Feichtner, O. Selig, M. Kiunke, B.J.P.r. l. Hecht, Evolutionary optimization of optical antennas 109(12) 127701 2012.

[9] S. Shriwastava, C.C. Tripathi, Metal–insulator–metal diodes: a potential high frequency rectifier for rectenna application, J. Electron. Mater. 48 (5) (2019) 2635–2652.

[10] A.Y. Elsharabasy, A.H. Alshehri, M.H. Bakr, M.J. Deen, K.P. Musselman, M. Yavuz, Near zero-bias MIIM diode based on TiO2/ZnO for energy harvesting applications, AIP Adv. 9 (11) (2019) 115207.

[11] H. Fischer, O.J.J.O.e. Martin, Engineering the optical response of plasmonic nanoantennas 16(12) (2008) 9144-9154.

[12] M.A. Seo, H.R. Park, S.M. Koo, D.J. Park, J.H. Kang, O.K. Suwal, S.S. Choi, P.C.M. Planken, G.S. Park, N.K. Park, Q.H. Park, D.S. Kim, Terahertz field enhancement by a metallic nano slit operating beyond the skin-depth limit, Terahertz field enhancement by a metallic nano slit operating beyond the skin-depth limit 3 (3) (2009) 152–156.

[13] A. Sundaramurthy, K. Crozier, G. Kino, D. Fromm, P. Schuck, W.J.P.R.B. Moerner, Field enhancement and gap-dependent resonance in a system of two opposing tip-to-tip Au nanotriangles 72(16) (2005)165409.

[14] J.M. McMahon et al., Gold nanoparticle dimer plasmonics: finite element method calculations of the electromagnetic enhancement to surface-enhanced Raman spectroscopy 394(7) (2009) 1819-1825.

[15] C. Feuillet-Palma, Y. Todorov, A. Vasanelli, C. Sirtori, Strong near field enhancement in THz nano-antenna arrays, Sci. Rep. 3 (1) (2013) 1361.

[16] T.A. Elwi, A.M. Al-Saegh, Further realization of a flexible metamaterial-based antenna on indium nickel oxide polymerized palm fiber substrates for RF energy harvesting, Int. J. Microwave Wireless Technol. 13 (1) (2021) 67–75.

[17] T.A. Elwi, D.A. Jassim, H.H. Mohammed, Novel miniaturized folded UWB microstrip antenna-based metamaterial for RF energy harvesting, Int. J. Commun. Syst. 33 (6) (2020) e4305, https://doi.org/10.1002/dac.4305.

[18] T.A. Elwi, Z.A. Abdul Hassain, O.A. Tawfeeq, Hilbert metamaterial printed antenna based on organic substrates for energy harvesting, IET Microwaves Antennas Propagat. 13 (12) (2019) 2185–2192.

[19] T.A. Elwi, Novel UWB printed metamaterial microstrip antenna based organic substrates for RF-energy harvesting applications, AEU – Int. J. Electron. Commun. 101 (2019) 44–53.

[20] S. Shen, C.-Y. Chiu, R.D. Murch, Multiport pixel rectenna for ambient RF energy harvesting, IEEE Trans. Antennas Propag. 66 (2) (2018) 644–656.

[21] S. Kim et al, Ambient RF Energy-Harvesting Technologies for Self-Sustainable Standalone Wireless Sensor Platforms, Proc. IEEE 102 (11) (2014) 1649–1666.

[22] M. Arrawatia, M.S. Baghini, G. Kumar, Broadband bent triangular omnidirectional antenna for RF energy harvesting, IEEE Antennas Wirel. Propag. Lett. 15 (2016) 36–39.

[23] A.Y. Elsharabasy, A.S. Negm, M.H. Bakr, M.J. Deen, Global optimization of rectennas for IR energy harvesting at 10.6 μm, IEEE J. Photovoltaics 9 (5) (2019) 1232–1239.

[24] I. Wilke, Y. Oppliger, W. Herrmann, F.J.A. P. A. Kneubühl, Nanometer thin-film Ni-NiO-Ni diodes for 30 THz radiation 58 (4) (1994) 329-341.

[25] M. Abdel-Rahman, F. González, G.J.E.L. Boreman, Antenna-coupled metal-oxide-metal diodes for dual-band detection at 92.5 GHz and 28 THz 40(2) (2004) 116-118.

[26] Kwangsik Choi, F. Yesilkoy, A. Chryssis, M. Dagenais, M. Peckerar, New process development for planar-type CIC tunneling diodes, IEEE Electron Device Lett. 31 (8) (2010) 809–811.

[27] Z. Zhu, S. Joshi, S. Grover, G. J. J. o. P. D. A. P. Moddel, Graphene geometric diodes for terahertz rectennas 46(18) (2013) 185101.

[28] P. Esfandiari et al., ''Tunable antenna-coupled metal-oxide-metal (MOM) uncooled IR detector, in Infrared Technology and Applications XXXI, 2005, vol. 5783, pp. 470-482: International Society for Optics and Photonics.

[29] S. Krishnan, H. La Rosa, E. Stefanakos, S. Bhansali, K.J.S. Buckle, A.A. Physical, Design and development of batch fabricatable metal–insulator–metal diode and microstrip slot antenna as rectenna elements 142(1) (2008) 40-47.

[30] J.A. Bean, A. Weeks, G.D.J.I.J.o.Q.E. Boreman, Performance optimization of antenna-coupled Al/AlOx/Pt tunnel diode infrared detectors 47(1) (2010) 126-135.

[31] S. Zhang, L. Wang, C. Xu, D. Li, L. Chen, D.J.E.S.S.L. Yang, Fabrication of Ni-NiO-Cu metal-insulator-metal tunnel diodes via anodic aluminum oxide templates 2(1) (2012) Q1.

[32] E.C. Kinzel, R.L. Brown, J.C. Ginn, B.A. Lail, B.A. Slovick, G. D. Boreman, Design of an MOM diode-coupled frequency-selective surface, Design of an MOM Diode-coupled Frequency-selective surface 55 (3) (2013) 489–493.

[33] S. Grover, G. Moddel, Engineering the current–voltage characteristics of metal–insulator–metal diodes using double-insulator tunnel barriers, Solid-State Electron. 67 (1) (2012) 94–99.

[34] A. Dhiflaoui, L. Ladhar, M. Aseeri, T. Aguili, N. Eltresy, and H. Rmili, ''Design of a Wideband and High directive Log Spiral THz Antenna for Photoconductive Sources, in: 2018 International Conference on Internet of Things, Embedded Systems and Communications (IINTEC), 2018, pp. 64-67.

[35] X. Zhang, C. Ruan, J. Dai, Study of terminal truncation on log-spiral antenna characteristics at terahertz frequency, in: 2017 Progress in Electromagnetics Research Symposium - Fall (PIERS - FALL), 2017, pp. 1445-1448.

[36] W. Miao, Y. Delorme, F. Dauplay, G. Beaudin, Q.J. Yao, S.C. Shi, Simulation of an integrated log-spiral antenna at terahertz, in: 2008 8th International Symposium on Antennas, Propagation and EM Theory, 2008, pp. 58–61.

[37] S.-K. Hong, K.-H. Yeon, S.W. Nam, S. Zhang, Exciton dynamics in a nanocrystal chain with a ring, Phys. Lett. A 360 (1) (2006) 1–5.

[38] R.E. Brandt et al, Band offsets of n-type electron-selective contacts on cuprous oxide (Cu2O) for photovoltaics, Appl. Phys. Lett. 105 (26) (2014) 263901.

[39] B. Chih-ming Lai, N.-H. Kung, J. Ya-min Lee, A study on the capacitance–voltage characteristics of metal-Ta2O5-silicon capacitors for very large scale integration metal-oxide-semiconductor gate oxide applications, J. Appl. Phys. 85 (8) (1999) 4087–4090.

[40] X. Liu, S. Wang, J. Zhang, J. Zhang, Y. Gu, Photoelectric properties and charge dynamics in ZnO nanowires/Cu4Bi4S9 and ZnO nanowires/In2O3/Cu4Bi4S9 heterostructures, J. Appl. Phys. 116 (24) (2014) 245101.

[41] A. Sanchez, C.F. Davis, K.C. Liu, A. Javan, The MOM tunneling diode: theoretical estimate of its performance at microwave and infrared frequencies, J. Appl. Phys. 49 (10) (1978) 5270–5277.

[42] K. Mistry, M. Yavuz, K.P. Musselman, Simulated electron affinity tuning in metal-insulator-metal (MIM) diodes, J. Appl. Phys. 121 (18) (2017) 184504.

[43] J.G. Simmons, Generalized formula for the electric tunnel effect between similar electrodes separated by a thin insulating film, J. Appl. Phys. 34 (6) (1963) 1793–1803.

[44] I.E. Hashem, N.H. Rafat, E.A. Soliman, Theoretical study of metal-insulator-metal tunneling diode figures of merit, IEEE J. Quantum Electron. 49 (1) (2013) 72–79.